Stator Winding Fault Thermal Signature Monitoring and Analysis by *In Situ* FBG Sensors

Anees Mohammed, *Student Member, IEEE*, Juan I. Melecio, and Siniša Djurović, *Member, IEEE*

***Abstract*—Winding short circuit faults are recognized as one of most frequent electric machine failure modes. Effective on-line diagnosis of these is vital, but remains a challenging task, in particular, at incipient fault stage. This paper reports a novel technique for on-line detection of incipient stator short circuit faults in random wound electrical machines based on *in situ* monitoring of windings thermal signature using electrically nonconductive and electromagnetic interference immune fiber-Bragg grating (FBG) temperature sensors. The presented method employs distributed thermal monitoring, based on the FBG multiplexing feature, in a variety of points within windings, in proximity to thermal hot spots of interest that arise from fault. The ability of the proposed method to enable fault diagnosis through identification of fault-induced localized thermal excitation is validated in steady-state and transient operating conditions on a purpose built inverter driven induction machine test facility. The results demonstrate the capability of unambiguous detection of inter-turn faults, including a single shorted turn. Furthermore, the winding thermal and electrical characteristics at the onset of inter-turn fault are examined and correlated, enabling better understanding of fault diagnostic requirements.**

***Index Terms*—Fiber-Bragg grating (FBG) sensor, in-situ thermal monitoring, inter-turn fault detection, inverter driven induction motor.**

I. Introduction

WINDING short circuit faults are one of most common occurring in electrical machines, especially in those utilizing random wound winding configurations. Short circuit related faults are reported to account for ≈30%–40% of total machine failures [1], [2]. The main cause of these is insulation material breakdown, occurring as a result of a combination of stresses (thermal, electrical, mechanical, and environmental) acting on windings during their operating life [1]. This insulation breakdown results in inter-turn short circuit fault (ITSCF), which in turn gives rise to further excessive thermal excitation in windings and ultimately leads to their failure. In-service detection of incipient stage ITSCF is thus vital as it could enable prevention of critical damage and reduction of the associated repair costs and production losses.

Research on stator winding ITSCFs detection has received significant attention and a range of diagnostic techniques suggested in literature [1]–[9]. These, in general, rely on noninvasive on-line monitoring and analysis of electrical and/or electromagnetic quantities, such as stator current, voltage, impedance, or flux. The reported techniques can however impose significant drawbacks in diagnostic capability and are particularly limited in effective recognition of early fault stages; for instance, minor changes in operating conditions, such as load variation, supply unbalance and inherent asymmetry, in particular at nonstationary conditions, can greatly affect their diagnostic performance [1], [10]. Additional drawbacks are posed by the challenges of fault location and fault severity diagnosis [10]. To overcome these, advanced processing of diagnostic signals is required, further complicating the implementation of the diagnostic process [3].

Thermal monitoring methods for ITSCF detection have not been widely investigated, mainly due to unavailability of adequate *in situ* winding thermal sensing technology and the lack of understanding of fault-induced thermal stress propagation. A few studies examine ITSCF diagnosis using thermographic analysis, where thermal imaging is used to monitor the machine frame in order to observe thermal hot spots induced by winding faults internal to machine structure [11]–[13]. While this approach does not allow fast recognition of *in situ* fault effects and hence rapid and timely diagnostics, and the recognition of incipient fault stages, it has been used to detect ITSCF in induction machines (IMs) with fault severity of 16% and above [11]–[13].

The duration of the transition period from the instant of ITSCF onset to that of machine breakdown is still not fully understood [4], [7], [9]. A model study in [8] has shown that an ITSCF in a 15-kw IM could develop to phase-to-ground fault in less than 5 s. However, the model reported in [8] assumed that there is no heat transfer from the faulty coil to the ambient, which may not be the case in a practical fault scenario. Experimental studies of realistic, practical inter-turn fault conditions in IMs rated at 3.7, 2.2, and 11 kW, respectively, are reported in [14]–[16]. The three studies recorded different transition times from the incipient inter-turn fault stage to phase-to-ground fault: In [14], the IM takes about 20 s to breakdown, while in [15] the recorded

Manuscript received April 25, 2018; revised August 1, 2018 and October 9, 2018; accepted November 4, 2018. Date of publication December 18, 2018; date of current version May 31, 2019. This work was supported by the U.K. Engineering and Physical Sciences Research Council (EPSRC) HOME-Offshore: Holistic Operation and Maintenance for Energy from Offshore Wind Farms Consortium under Grant EP/P009743/1. *(Corresponding author: Siniša Djurović.)*

The authors are with the School of Electrical and Electronic Engineering at University of Manchester, M13 9PL, Manchester, U.K. (e-mail: anees.mohammed@manchester.ac.uk; Ignacio.melecio@manchester.ac.uk; sinisa.durovic@manchester.ac.uk).

Color versions of one or more of the figures in this paper are available online at http://ieeexplore.ieee.org.

Digital Object Identifier 10.1109/TIE.2018.2883260

breakdown time was 5.5 h and in [16] 15 min. While there are many complex factors depending on machine design, rating, and operating conditions that determine the fault transition period, it can generally be concluded that the short circuit fault propagation time is challenging to evaluate and can vary from seconds to hours [14]–[16] or even days and months [4], [7]. However, the excessive winding thermal hot spots induced by this type of faults and their propagation can be considered the main factor that characterizes this transition. This localized excess heat is rapidly induced in the shorted turns and thus, if monitored appropriately, could be used as an effective diagnostic tool. In fact, knowledge of the fault-induced thermal excitation can be used not only for fault detection, but it can also help to estimate the time to reach critical insulation breakdown temperatures of the adjacent healthy turns, which is crucial to determine the time available for corrective action to be applied. Such diagnostic knowledge would be highly valuable in critical electrical machine applications, such as in air and ground electric vehicles or offshore wind generation.

This paper reports a proof of concept study of a new technique for on-line detection of ITSCFs in random wound electrical machines based on winding *in situ* thermal signature monitoring using coil embedded fiber-Bragg grating (FBG) temperature sensors. FBG sensing technology provides a number of advantages over electrical machine conventional sensing technologies, making it an attractive candidate for facilitating operative condition monitoring solutions. FBG sensors are characterized by inherent electromagnetic interference (EMI) immunity, robustness, multiplexing, small size, and multiphysical sensing features [17], [24]. From the machine application point of view, FBG sensing is an invasive monitoring technique; thus the cost and complexity of installation could potentially be considered as its drawbacks. In principle, the FBG monitoring system architecture follows the general structure of commercial condition monitoring systems used for electrical machines/drive trains, requiring a suite of dedicated sensors and a hardware device to enable interpretation, monitoring, and analysis of sensed diagnostic signals [25]. The FBG sensor cost is currently comparable to cost of conventional thermal sensors used in electric machine applications, but the required FBG interrogator systems remain relatively costly. FBG sensing technology has already found use in aerospace and wind industries where its features have contributed to development of more effective monitoring systems [25]–[27]. The application of FBG thermal sensors in electric machines has recently been examined and techniques developed and validated that enable effective FBG thermal sensing application within random wound windings [20]–[24].

In this paper, a series of experimental tests were carried out to examine the potential of using targeted, *in situ*, FBG enabled thermal monitoring for diagnosis of ITSCF with a particular focus on the critical, incipient fault stages. To this end, a number of FBG temperature sensors were embedded in points of interest of an inverter driven test IM stator windings. The test machine was rewound to enable the installation of *in situ* sensors and its windings modified to facilitate practical emulation of ITSCF. The diagnostic potential of *in situ* monitored ITSCF thermal signature was examined in steady-state and transient operating conditions; the method enables effective diagnosis of early stage ITSCF (i.e., single turn), as well as fault severity diagnosis and fault location identification. In addition, the electrical and thermal characteristics of stator windings during an inter-turn fault event are examined and correlated and it was shown that clearer understanding of these can significantly contribute to fault diagnostic reliability.

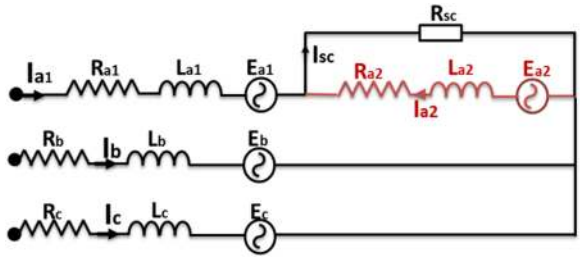

Fig. 1. IM stator winding under inter-turn fault.

II. Analysis of ITSCF Electrothermal Features

Winding faults almost invariably propagate from an ITSCF, when insulation breaks down between two adjacent turns of the same coil; the direct electrical contact between these causes a high circulating current, which gives rise to localized excessive heat in the faulty winding part, i.e., in the shorted turns [2], [3]. The resulting high temperature in turn degrades the insulation of neighboring healthy turns, thus involving more turns in the fault as a consequence. If ITSCF is not detected and remedied in early stages, this process propagates and deteriorates the surrounding healthy winding insulation [4], [5], initiating further fault expansion and leading to more significant, phase-to-phase or phase-to-ground faults, and ultimately machine failure. Detecting fault in incipient stage is therefore key in avoiding potentially catastrophic damage to operating machines. The electrothermal features of ITSCF are analyzed in this section as an enabler to understanding the requirements and challenges of its diagnosis based on thermal and/or electrical signal analysis.

A. Electrical Characteristics of Inter-Turn Fault

The electrical circuit diagram in Fig. 1 shows a three-phase stator winding under ITSCF condition assumed in phase A. The ITSCF modifies the faulty phase into two separate electrical circuits: One formed by the healthy winding portion and the other by the winding conductors encompassed by fault. The resistances and inductances of the healthy and faulty circuits depend on the faulty N_F, to healthy N_H, turns number ratio μ, where $\mu = N_F \backslash N_H$ [7].

The two circuits are electrically independent and magnetically coupled, and are established as follows: When the ITSCF occurs, the shorted turns physically act as a shorted coil placed in the machine main magnetic field path, as shown in Fig. 2(a). An electromotive force (Ea2) is thus induced in these driving a fault current (Ia2) [8]. Due to Lenz's law, the fault current establishes a flux opposing that of the main field, consequently reducing it along the faulty coils, and in turn reducing Ea2. Another effect reducing Ea2 is the main magnetomotive force (MMF)

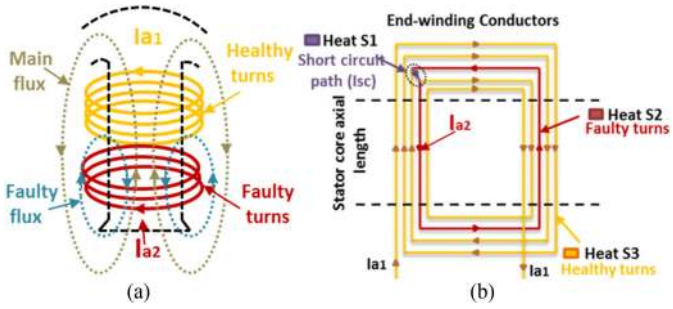

Fig. 2. Winding coil with inter-turn fault.

reduction due to fault-induced reduction of ampere/turns in the faulty phase [8], [9]. As shown in Fig. 2(a) and (b), the faulty turn current Ia2 is in opposite direction to healthy winding portion current Ia1 and is determined by the impedance of the short circuited turns and Ea2 [5]. Ia2 can thus vary significantly and is challenging to determine; recent studies have reported it possible for it to be up to 12 times the magnitude of machine rated current [6]. Ia1 on the other hand is mainly affected by the phase impedance which varies with μ.

ITSCF detection using electrical or magnetic signals generally depends on identifying effects caused by two distinct electromagnetic features of an ITSCF event [28]: The first is the air-gap field distortion caused by shorted turns and the consequent MMF reduction, while the second is the fault-induced phase impedance asymmetry giving rise to phase currents imbalance. However, in ITSCF, low severity events encompassing a single or a few turns, which characterize fault incipient stage, these effects are typically insignificant. This illustrates the inherent complexity of incipient ITSCF detection using electromagnetic signature analysis.

B. Thermal Characteristics of Inter-Turn Fault

1) Inter-Turn Fault-Induced Heat Thermal Analysis: In healthy conditions, the heat generated in the stator winding is a result of the ohmic losses, determined by winding current and resistance, and dissipated as heat to the surrounding ambient. In a conventional balanced machine, the ohmic losses induced by each stator phase winding are, in general, almost equal. This results in an even generation and dissipation of heat in the winding, and hence an even temperature distribution. In ITSCF conditions, due to the high fault current circulating in the shorted turns, a faulty coil will generate higher ohmic loss compared to healthy coils. This will result in a localized thermal hot spot in the winding where the fault is occurring. Therefore, understanding the thermal behavior of the faulty coil is key to understanding the thermal monitoring requirements for fault diagnostic purposes.

The ITSCF starts when local insulation breakdown occurs between two adjacent turns in a coil. This breakdown can occur at any location in the coil structure, i.e., in the coil sides (slot section) or in the coil ends (end-winding section). At the breakdown location a high short circuit current (I_{SC}) flows between the shorted turns that is generally equal to the sum of the phase current and the shorted turns current [8], shown in Fig. 1. The

TABLE I
HEAT LOSS CALCULATION IN HEALTHY AND FAULTY COILS

Healthy coil	$\text{Heat}= \left(I_{phase} \right)^2 x\, R_{Coil}$	(1)
Faulty coil	$\text{Heat S1} = \left(I_{sc} \right)^2 x\, R_{sc}\,.$	(2)
	$\text{Heat S2} = \left(I_{a2} \right)^2 x\, R_{a2}, \quad R_{a2} = \mu\, R_{Coil}$	(3)
	$\text{Heat S3} = \left(I_{a1} \right)^2 x\, R_{a1}, \quad R_{a1} = (1-\mu) R_{Coil}$	(4)

I_{SC} and the contact resistance (Rsc) between shorted turns generate heat at the contact location in the faulty coil, denoted as heat source 1 (Heat S1). The second source of heat (Heat S2) induced in the faulty coil arises due to high current (Ia2) in the shorted turns and their resistance (Ra2); Heat S2 acts along the shorted turn length and hence along the faulty coil structure. The healthy turns' resistance (Ra1) and current (Ia1) determine a third source of heat (Heat S3). Table I summarizes the calculation of heat loss components in a coil under healthy and ITSCF conditions.

The heat loss in the faulty coil is seen to be defined by a range of quantities, such as Ia1, Ia2, Isc, and μ. These will vary with fault severity and operating condition variation, e.g., fault propagation and changes in motor load and/or speed/frequency. As the fault-induced heat loss largely determines the fault-induced thermal signature, the thermal signature of a faulty coil will also vary with fault severity and load and speed variation. In general, as winding fault propagates (i.e., fault severity is increased) the number of shorted turns N_F, and hence μ, increases; this leads to increase of the shorted turns induced voltage Ea2, and consequently the shorted turns current Ia2. The faulty coil healthy turns N_H are consequently reduced, resulting in a reduction of the healthy turns' resistance Ra1. The reduction in Ra1 increases the phase current Ia1 and hence the loss in the healthy coils of the faulty phase. At high fault severities, this can result in an uneven temperature distribution between winding phases and increase in thermal stress in the healthy part of the winding. On the other hand, with load variation (i.e., load increase) the winding operating temperature increases due to increase in the phase current Ia1 and the heat loss it generates. Consequently, Ra1 and Ra2 will also increase due to copper electric resistance temperature dependency. The change in these resistances will yield a change in corresponding currents Ia1 and Ia2 and the associated fault-induced heat losses. Finally, variable speed operation, such as applied under variable frequency drive motor control, can directly affect the shorted turn induced voltage Ea2. The variation in Ea2 with speed variation will lead to variation in Ia2 and hence in fault-induced heat. In summary, understanding the heat losses dependence on fault severity and machine operating conditions is valuable for thermal signature based diagnostics. In this respect, identification of consistent thermal signature variation patterns with fault and load variation would underpin consistent thermal signature based winding fault diagnosis for an arbitrary machine design and operating condition.

2) Inter-Turn Fault-Induced Heat Monitoring Requirement: From the point of *in situ* thermal monitoring and instrumentation for winding fault diagnostic purposes, Heat S1 is extremely challenging to monitor, as it can occur at any point

of the winding structure. In addition, the fault contact resistance Rsc can be assumed very small and is hence generally not expected to be the dominant component of thermal excitation originating from a fault event. Heat S2 generated by Ia2 is generally expected to produce a more significant contribution to total fault-induced thermal excitation, and therefore a more significant detriment to winding health, and the neighboring healthy turns in particular. The resulting excess Heat S2 acts in the shorted turns along the coil length [see Fig. 2(b)]. While monitoring end winding temperature is common and specified in thermal management standards of electrical machines [29], the end windings generally act as a single thermal component combining all coil ends and thus any temperature measurement in these largely yields an average temperature reading of all coil ends temperatures. Monitoring thermal changes induced at outset of an ITSCF event in end windings would therefore not be effective for diagnostic purposes. Monitoring thermal excitation in any of the faulty coil sides would, on the other hand, enable the measurement of fault-induced thermal excitation, as this is localized within the slot section and acts along the core axial length; this approach would facilitate *in situ* thermal monitoring enabled ITSCF fault diagnosis.

In the slot section, the fault can occur at any position, thus understanding the sensing placement in the slot cross section that yields optimal performance is key. From the heat transfer point of view, the slot center has the highest sensitivity to any thermal variation in the slot area. This is due to the fact that the heat in the slot transfers from conductors toward slot walls, to the adjacent teeth and core yoke. However, as result of the slow heat transfer process between the winding and the stator core structure surrounding it due to the presence of the slot liner, a temperature gradient is generated in the slot section with highest temperature in the slot center. Therefore, in case where any additional heat source is induced in the heat transfer path between the slot center (hot spot) and slot walls, such as in case of an ITSCF, will slow the heat transfer rate from the slot center and hence increase its temperature. Consequently, enabling thermal monitoring in the slot section hot spot location would provide the most effective means to detect fault-induced thermal variation, short of installing *in situ* sensors to cover the entirety of the slot cross-sectional area, which would be prohibitive in practical applications. Furthermore, locating the thermal sensor in the slot center between the copper conductors ensure that it is positioned at an optimal point in terms of distance from all possible fault locations in the slot winding and therefore yields optimal recognition response of the fault thermal signature assuming use of a single sensor. In addition to this, for healthy motor operation monitoring of winding thermal hot spots is key to understanding efficacy of machine utilization and can enable development of winding life estimation routines [30]. A single thermal sensing point in the slot center hot spot location would therefore enable recognition of ITSCF thermal signature.

To understand thermal behavior in a single slot section Table II defines heat loss calculation under healthy and faulty conditions. The total heat loss in the slot section under fault conditions can be calculated based on the current in the healthy and faulty turns and the conductor electrical resistance per core

TABLE II
HEAT CALCULATION IN THE SLOT SECTION

Heat in healthy condition	$I^2_{phase}\ x\ R_{slot-axial\ lenght}\ x\ N_H$	(4)
Heat in faulty condition	$I^2_{a2}\ x\ R_{slot-axial\ lenght}\ x\ N_F$	(5)
	$I^2_{a1}\ x\ R_{slot-axial\ lenght}\ x\ N_H$	(6)

TABLE III
TEST MOTOR SPECIFICATION

Examined IM data	
Rated power/voltage/current	0.55 kW/400 V/1.6A
Efficiency, efficiency class	66 %, IE1
Rated speed/pole number	1380 rpm/4
Magnetisation current	1.1A
Cooling method	IC 41
Slot number stator/rotor	24/30
Insulation class	F
Temperature rise class	B
Duty cycle type rating	S1

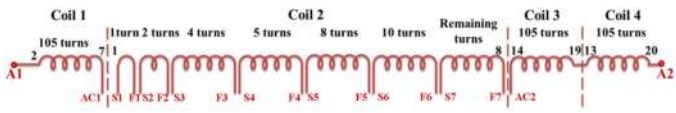

Fig. 3. Modified stator phase for winding ITSCF emulation.

axial length ($R_{\text{slot}-\text{axiallength}}$). Based on the above analysis, the ability to measure even small excursions in winding slot section temperature can enable the detection of possible problems in the winding due to faults at an early stage. Therefore, this study reports an *in situ* thermal sensing scheme to enable monitoring of slot section hotspots that originate from winding fault, and therefore its diagnosis.

III. EXPERIMENTAL TEST RIG DESCRIPTION

The proposed stator winding fault on-line diagnostic technique based on *in situ* thermal signature was established by installing a number of FBG probes into a 0.55-kw/three-phase cage rotor IM. The examined motor specifications are provided in Table III.

The stator was rewound to enable sensor installation in target positions and ITSCF experimental emulation. Windings were modified to allow emulation of a range of single or multiple turn faults by tapping specific phase A winding points, as shown in Fig. 3. The test motor phase windings consist of four series-connected coils, each with 105 turns of 24 AWG enameled copper wire. The fault location is arbitrarily chosen to be in coil 2 of phase A. The practically examined ITSCF severities defined as percentage ratio of winding shorted and effective turns are presented in Table IV. The maximum examined fault severity is 2.38% as this study focuses on detection of incipient stages of ITSCFs.

Fig. 4 shows the embedded thermal sensor locations in the test machine. Based on the thermal sensing requirements for ITSCF detection discussed in Section II-B, at least one *in situ*

TABLE IV
INVESTIGATED INTER-TURN FAULT SEVERITY

Turns	1	2	3	4	5	8	10
Severity %	0.23	0.47	0.71	0.95	1.19	1.9	2.38

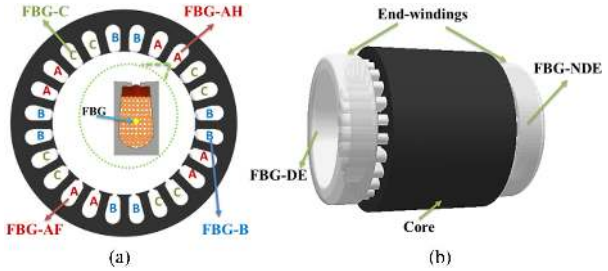

Fig. 4. Test motor thermal sensor positions. (a) FBG sensor locations in slot sections. (b) FBG locations in end-winding sections.

thermal sensor per coil is required to cater for the diagnostic of the entire winding. However, the aim of this feasibility study is to demonstrate the viability of *in situ* FBG thermal sensing concept for ITSCF detection: To this end, an array FBG sensor containing four FBG heads was embedded and distributed in four known healthy and faulty slots, Fig. 4(a). The *in situ* sensor was designed following the principles put forward in [22]–[24]: The individual FBG head length is 5 mm, imprinted in bend insensitive polyimide single mode fiber with average bandwidth of ≈0.34 nm, reflectivity of ≈80%, and sensitivity of ≈12 pm/°C. The central Bragg wavelength of each FBG head is 1554.684, 1549.962, 15544.930, and 1539.881 nm, respectively. The FBG heads are packaged in a polyetheretherketone (PEEK) capillary to eliminate external mechanical excitation, while the remainder of the optic cable is tubed in Teflon for protective purposes. PEEK is electrically nonconductive and EMI immune and can withstand operating temperatures in excess of ≈300 °C. The utilized sensor design has been shown to provide reliable measurement of winding thermal rise rates of up to ≈55 °C/s with measurement error lower than 1 °C [24].

Each FBG head was placed between copper conductors in the slot center, following installation principles in [22]–[24]. The FBGs were positioned to enable thermal monitoring of an emulated fault location and a uniform thermal sensing distribution within the examined motor geometry. Two FBG heads were thus installed in slots containing phase A coils, one (FBG-AH) in the slot containing a healthy coil side and the other in the slot that contains the faulty coil side (FBG-AF). The two remaining FBG heads (FBG-B and FBG-C) were installed in slots containing coils of healthy phases B and C, respectively. In addition to the FBG array sensor, two single FBG sensors were installed to monitor the end windings: One was embedded in the drive-end winding (FBG-DE) and another in the nondrive end winding (FBG-NDE), Fig. 4(b).

The performance of the proposed scheme was examined in experiments on a laboratory test rig. Fig. 5(a) gives the schematic diagram of the test rig configuration, and Fig. 5(b) shows a photograph of the actual test rig. The prototype FBG instrumented IM was coupled to a permanent magnet direct current machine load machine whose armature current was regulated using a controllable resistive load bank. The IM was supplied by a three-phase Parker SSD890 ac drive operating in open-loop (V/f) control mode. The phase A current and the shorted turns circulating current and voltage were monitored by LeCroy CP150 current probes and a LeCroy ADP300 voltage probe in the tests. Instantaneous currents and voltage were 2synchronously recorded using a LeCroy 434 digital oscilloscope. The FBG sensors were illuminated using a broadband light source provided by a commercial multichannel (SmartScan04) interrogator unit. The monitored FBG wavelengths were processed using the LabVIEW-based SmartSoft software.

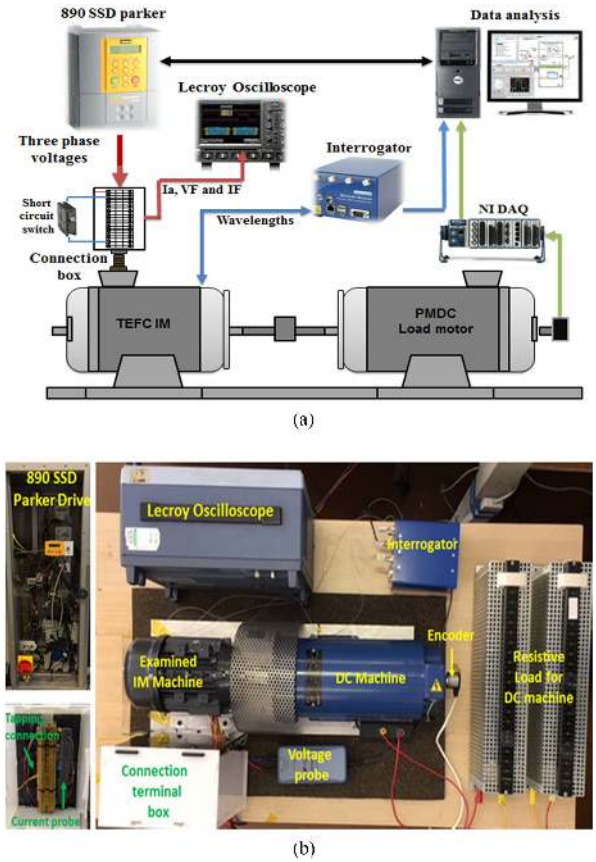

Fig. 5. Experimental test rig setup. (a) Experimental test rig configuration. (b) Photograph of the test rig.

IV. EXPERIMENTAL RESULTS AND DISCUSSION

An experimental study undertaken to evaluate the application of the proposed *in situ* thermal monitoring scheme for incipient ITSCF diagnosis on the inverted driven IM test rig is reported in this section. The study also includes an analysis of electrothermal characteristics of the test motor operating in early stages of ITSCF. Signature of fault severities ranging from a single to ten shorted turns is examined under steady-state and transient thermal conditions at different operating frequencies in *V/f* control mode.

A. Fault Thermal Signature in Steady-State Conditions

1) Base Frequency Conditions: This section studies the efficacy of fault diagnosis in steady-state thermal conditions.

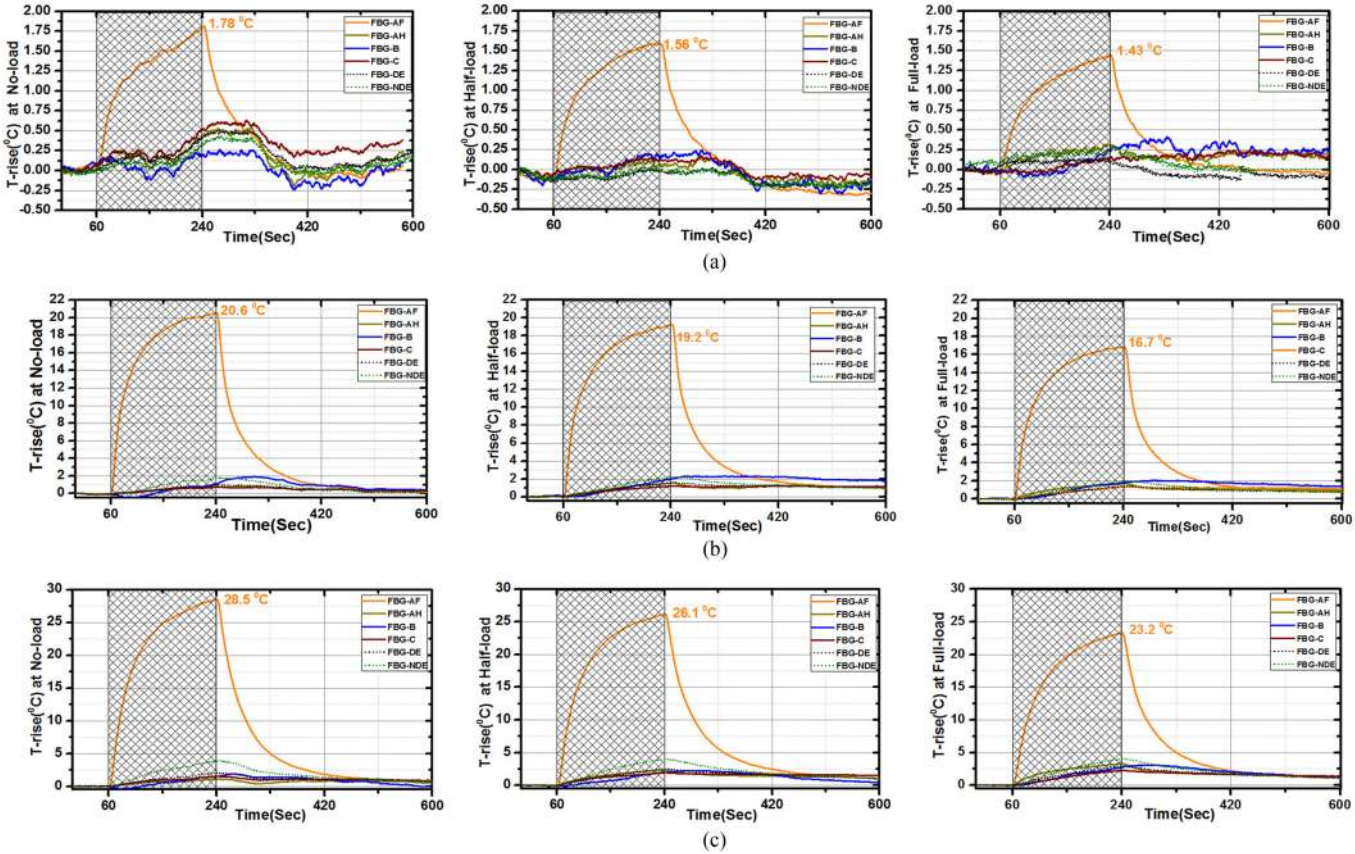

Fig. 6. Measured temperature rise profiles under ITSCF condition. (a) Measured temperature rise with single turn short circuit fault. (b) Measured temperature rise with five turn short circuited. (c) Measured temperature rise with ten turn short circuited.

To this end, an ITSCF was emulated in the test machine after thermal equilibrium for a chosen operating point was reached. Fault severities of one, two, three, four, five, eight, and ten shorted turns were examined, as summarized in Table IV. For each considered fault, case tests were undertaken at a nominal supply frequency of 50 Hz and at no-load, half-load, and full-load conditions.

1) *Test procedure description*: The test procedure applied for each fault case and load condition involved waiting for the thermal equilibrium to first be achieved and then performing the following procedure. Healthy winding hot spot temperatures at thermal equilibrium were first monitored for 60 s. A short circuit fault is then induced and maintained for a period of 180 s within which thermal readings were taken. Finally, the fault is removed and thermal readings taken during cool down period and return to healthy winding thermal equilibrium. To practically emulate short circuit fault conditions as close as possible to those of actual fault, but without damaging the machine, the faulty turns were directly shorted in experiments using an electrical switch for fault tests of up to and including five shorted turns. Here the tapping leads and the switch resistance act as current limiters. In the tests involving eight and ten shorted turns, however, an additional resistance was added to limit the faulty current to 8 A in order to protect the motor. The 8-A short circuit current limit was set based on undertaking offline dc thermal excitation tests to rate thermal limits of the tested motor.

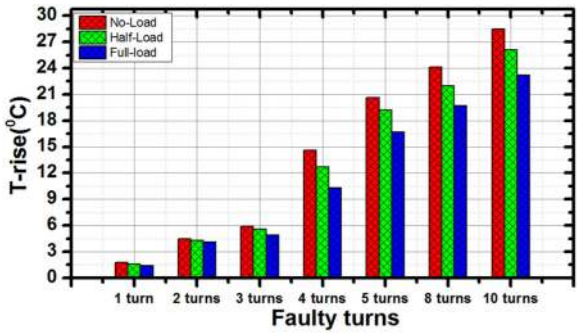

Fig. 7. Measured fault-induced temperature rise in steady-state conditions.

2) *In situ thermal signature monitoring performance*: For the sake of brevity, only the thermal measurements obtained by FBG sensors in one, five, and ten shorted turn tests are shown in Fig. 6. To clearly illustrate the observed thermal changes, the recorded thermal rise with respect to healthy thermal steady state is presented. The data demonstrate that the *in situ* FBG sensor (FBG-AF) in the faulty coil slot is able to instantaneously measure the additional thermal excitation arising from ITSCF. A temperature rise of 1.8 °C is recorded at the lowest case of

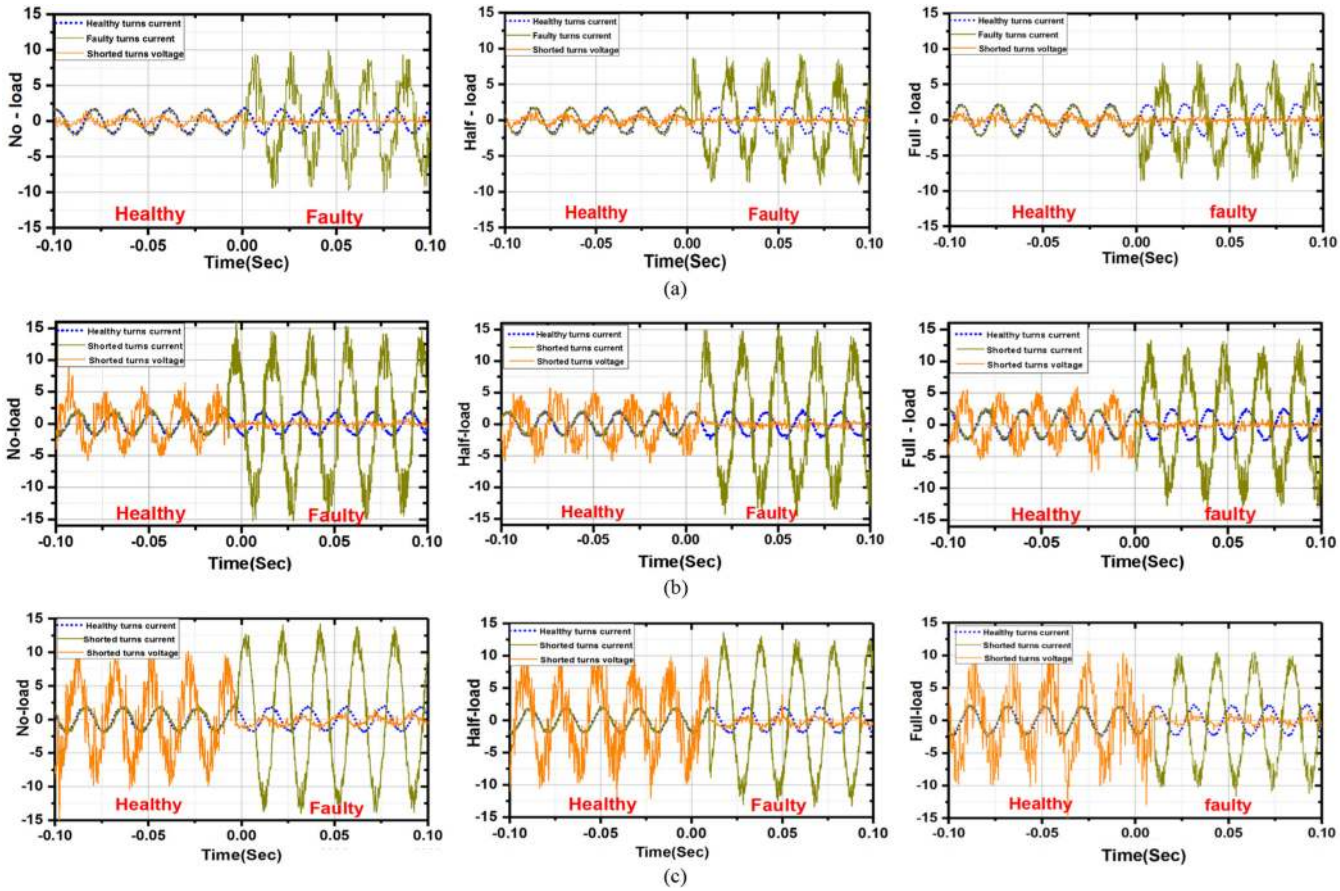

Fig. 8. Measured currents in healthy and faulty turns, induced voltage in shorted turns. (a) Measured currents in healthy and faulty turns, induced voltage in shorted turns in case of one shorted turn. (b) Measured currents in healthy and faulty turns, induced voltage in shorted turns in case of five shorted turn. (c) Measured currents in healthy and faulty turns, induced voltage in shorted turns in case of ten shorted turn.

fault severity (single turn) and around 28.5 °C at the highest examined fault severity (ten shorted turns). The other FBG sensors embedded in the healthy slots and in the end windings report insignificant thermal rise rates in comparison, as they are located away from the fault-induced localized thermal stress, as discussed in Section II-B-2. The ITSCF thermal signature is seen to be clearly distinguishable from the fault onset. The presented results highlight the high sensitivity of *in situ* FBG sensors and their capability of registering thermal variations as small as ≈0.2 °C between measurements under different load conditions, as observed in the single turn shorted fault case.

The experimental data in Fig. 6 clearly demonstrate the capability of the proposed *in situ* thermal monitoring scheme for detection of stator winding ITSCFs. It should be noted that the reported measurements were taken under constrained fault conditions in order to avoid test equipment damage. In a practical ITSCFs scenario, however, the fault currents will be higher and hence the fault thermal signature is expected to be even more obvious. As an illustration, considering a one turn fault in the examined motor with an assumed fault current of 12 times the rated current [6], this will generate ≈3.6 W of heat loss in the winding slot section containing a faulty coil side, according to (6) in Table II ($R_{\mathrm{slot-axial\,lenght}}$ in the examined machine is ≈ 0.01 Ω @ 25 °C). This is higher than the heat loss of ≈3.2 W produced by five shorted turns fault with an imposed 8-A fault current limit. It can thus be expected in a practical single short turn fault scenario to observe a temperature rise ≈20 °C or more higher than that was measured by the FBG-AF in the 5 shorted turns fault case.

1) *Thermal signature analysis*: To enable understanding of diagnostic potential the experimental results for fault thermal signature in Fig. 6 are examined with respect to fault severity and load dependency. The measured temperature rise and its rate of change reported by FBG-AF are seen to be significantly more affected by fault severity than by loading. On the other hand, it is interesting to observe that the amount of heat generated in the winding slot section containing a faulty coil side is reduced when the load increases, as evidenced by the measured temperature rise profiles for each considered ITSCF case summarized in Fig. 7. The examined fault severities are seen to exhibit a closely similar profile of thermal signature rise with load. The observed temperature rise presents a clear fault detection index, while the difference in thermal signature magnitude (i.e., column height in Fig. 7) provides a diagnostic index for fault mapping.

TABLE V
SHORTED TURNS CURRENT AND HEAT LOSS COMPONENTS FOR ALL FAULT CASES

Shorted turns number	Shorted turns current	Heat loss	Shorted turns current	Heat loss	Shorted turns current	Heat loss
	No-load		Half-load		Full-load	
	A	W	A	W	A	W
1	5	0.2885	4.7	0.26347	4.34	0.24279
2	7	1.13092	6.6	1.03908	6	0.92808
3	6.15	1.30941	5.7	1.16252	5.23	1.05774
4	8.3	3.17996	7.9	2.97746	7.3	2.74763
5	7.9	3.60106	7.5	3.35447	7.1	3.24892
8	7.8	5.61675	7.35	5.15461	6.75	4.69841
10	7.9	7.20211	7.38	6.49597	6.71	5.80361

For further understanding of observed fault thermal signature trends shown in Figs. 6 and 7 with respect to fault severity and load dependency, the winding electrothermal characteristics and the resulting fault-induced heat loss were analyzed. For this purpose, the currents in the healthy and faulty turns and the shorted turns voltage signals were synchronously measured for each fault case. For illustration purpose, Fig. 8 shows the obtained measurements in one, five, and ten shorted turn cases at different load conditions. The graphs show measurements in healthy conditions followed by a fault period. The measured shorted turn current (dark green trace) exhibits a sizable rise with fault application, with little noticeable change in healthy turn current (blue trace). Current levels of ≈1.6, ≈1.3, and ≈1.1 A were recorded for healthy operation under full, half, and no load conditions, respectively. The shorted turns current is seen to be phase shifted to the current in healthy turns and acts to reduce the shorted turns voltage induced in the shorted turns (orange trace) during a fault event. These measurements confirm the analysis of ITSCF electrical characteristics provided in Section II-A.

The rms values of the measured shorted turns current were used to determine the fault-induced heat loss in the slot section for each fault condition, using (6) in Table II. The $R_{\mathrm{slot-axiallength}}$ value was corrected for each load condition based on the measured winding operating temperature as follows: No-load resistance ≈0.1154 Ω @ 65 °C, half-load resistance ≈0. @ 74 °C, and full-load resistance ≈0.1289 Ω @ 97 °C. The measured shorted turns current values along with the associated fault-induced heat loss for all examined fault cases and loads are shown in Table V. The presented data show an increase in the shorted turns current and fault-induced heat loss with fault propagation and their clear decrease with load increase; for the shorted turn current, this trend is apparent in measurements shown in Fig. 8. The calculated fault-induced heat loss behavior can be directly linked to and clarifies the measured thermal signature profiles in Figs. 6 and 7, since these thermal profiles are determined by the amount of heat loss induced in the slot due to fault presence.

The increase in the fault-induced heat loss and hence fault-induced thermal signature rise with fault severity can be explained as follows: As severity increases, more shorted turns are involved in the fault, resulting in an increase of the shorted turn induced voltage. This in turn leads to an increase in the shorted turn current and hence the associated heat loss and thermal signature increase as shown in Table V and Fig. 7, respectively.

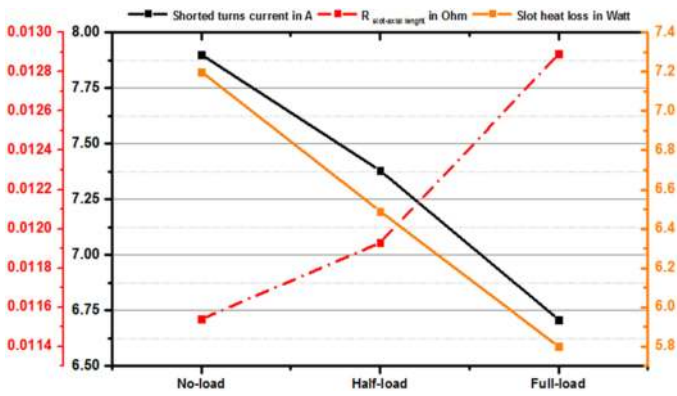

Fig. 9. Fault-induced heat loss, shorted turn current, and resistance variation with load, ten turns shorted fault.

On the other hand, the decrease in fault-induced heat loss (see Table V) and the corresponding thermal signature (see Fig. 7) with load increase can be explained by associated electrothermal effects. Fundamentally, the shorted turns current magnitude is determined by the values of shorted turn induced voltage and resistance. A load increase also increases the drawn phase current and hence winding loss and operating temperature, resulting in healthy and faulty turns resistance increase. The shorted turn resistance increase resulting from load rise will thus act to limit the shorted turn current which consequently decreases with load increase, as shown in Table V. This decrease is amplified to an extent by the minor decrease observed in the measured shorted turns voltage with load increase. While, in general, the shorted turn resistance increase would be expected to result in a heat loss increase in shorted turns; this loss is predominantly influenced by the more substantial shorted turn current reduction. To illustrate this, Fig. 9 shows the calculated fault-induced heat loss in the slot section for a 10 shorted turn fault case versus load along with the measured shorted turn current and $R_{\mathrm{slot-axiallength}}$. The data in Fig. 9 show that $R_{\mathrm{slot-axiallength}}$ is increased with load from ≈0.01154 at no load to ≈0.01289 Ω at full load due to operating temperature increase. The shorted turn current is consequently reduced from about ≈7.9 to ≈6.7 A. Crucially, the fault-induced heat loss reduces from ≈7.2 W at no load to ≈5.8 W at full load. In general, for an arbitrary number of shorted turns, the total shorted turns resistance increase due to load rise induced temperature increase is directly proportional to the number of turns shorted. This explains the difference in no load to full load temperature rise trends with fault severity observed in Fig. 7 and the heat calculations in Table V.

To examine the actual thermal stress related to thermal rise recordings in Fig. 7, the corresponding temperature measurements are shown in Fig. 10. It should be noted that the examined machine is an IE1 standard efficiency class design, meaning that it produces relatively high losses that significantly increase with loading. The relationship between loading and losses for IE1 design class is quadratic, and can be equally applied to the relationship between loading and temperature [31]; this is evident in the thermal measurement trends in Fig. 10, where the difference between no-load and full-load winding temperature is ≈35 °C. Although the temperature rise measured due to fault at no load

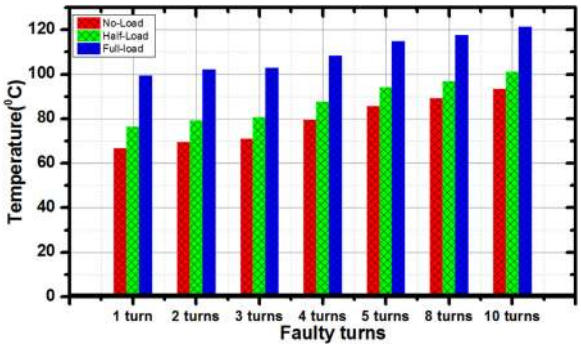

Fig. 10. ITSCF temperature measurements in steady-state conditions.

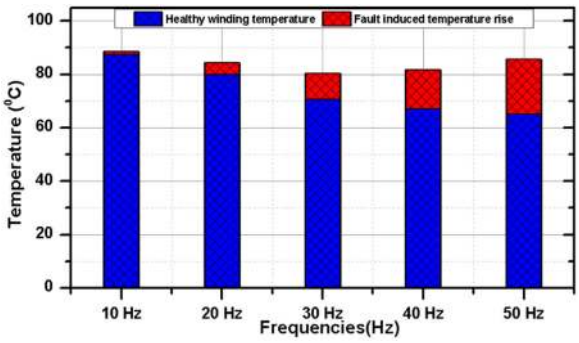

Fig. 11. FBG-AF measurements for different operating frequencies.

is higher than at full load (see Fig. 7), the winding thermal excitation is higher during fault at full load (see Fig. 10) due to the high operating temperature of ≈97 °C. However, in machines with higher efficiency classes, e.g., IE3 or IE4, this thermal behavior can differ and higher thermal stress due to ITSCF may occur at no-load conditions.

2) V/f Control Operating Frequency Change: ITSCF thermal signature recognition is examined in this section for the *V/f* controlled test machine operation at a range of different supply frequencies. The following five different operating points were assessed: 50 (base frequency) 40, 30, 20, and 10 Hz. A five shorted turn fault was experimentally tested under each of these frequencies. This is for the reason that the five turn fault emulation within nondestructive fault current limit constraints on the available laboratory system can be assumed approximately equivalent in terms of resulting thermal excitation to a practical single turn fault scenario, as discussed in Section IV-A. The tests were performed following an identical procedure to that described in Section IV-A-1. Tests were executed under no-load conditions in order to avoid overheating the examined motor winding due to the natural degradation of the cooling capability at low frequency operation for this motor design class. The thermal measurements obtained by FBG-FA are summarized in Fig. 11. Fig. 11 columns are divided into two areas: The blue area represents the healthy winding hot spot at thermal equilibrium for each operating frequency, while the red area is the measured hot spot temperature rise caused by fault.

The results show that as the operating frequency is reduced, the fault-induced thermal stress reduces as well, while the healthy, i.e., operational, thermal excitation increases. The *V/f* controlled IM drive operating factor that causes this behavior is the operating speed. The operating speed reduces with supply frequency reduction; this reduces the machine cooling system capability, as at reduced speeds, the motor becomes predominantly cooled by natural rather than forced convection. This cooling performance degradation with speed reduction yields an increase of the healthy winding temperature, seen to rise in the measured data from 65 °C at 50 Hz to 87.4 °C at 10 Hz. Conversely, the ITSCF-induced thermal rise is seen to reduce with operating frequency reduction, from 20.6 °C at 50 Hz to 1.2 °C at 10 Hz. This is largely due to the decrease of the induced shorted turn's voltage as result of reduction of the speed, but is further amplified by the winding temperature increase resulting in shorted turn resistance increase and thus fault current reduction. Most importantly, the data show that the same ITSCF condition can produce different thermal excitation levels at different operating frequencies due to winding electrothermal characteristics at fault outset; the fault-induced thermal stress is more significant at 10 and 50 Hz than at 20, 30, and 40 Hz in the examined system.

B. Fault Thermal Signature in Transient Conditions

This section examines the detection of ITSCF thermal signature in transient conditions. Transient conditions impose challenges as during these, stator current can increase to many times more than its steady-state value. The healthy winding temperature rise and its rate of change under such thermal transients could affect the diagnostic performance of the *in situ* FBG sensing system. To evaluate diagnostic performance in this respect, a cycling transient at 50 Hz is applied on the test machine under healthy and ITSCF conditions.

The examined thermal transient involved application of an S6 cycle to the test machine based on the IEC 60034-1 standard [29]. In this cycle, the motor was tested with a 125% load for 4 min followed by 6 min of no load operation. The cycle was controlled to keep the winding temperature rise above the ambient lower than the permissible temperature rise (80 °C, class B) for the examined motor. Once thermal equilibrium was reached under the applied cycle, a five shorted turns fault was introduced; two 60-s fault instances were examined within a single cycle, one within the cycle heating period and the other in the cycle cooling period. Fig. 12 shows the two applied cycle measurement without and with the inter-turn fault. In the heating period, the fault was applied at the instant of loading (i.e., heating period start), which is assumed to be the most difficult instant to distinguish healthy and faulty thermal profiles as all sensors inherently record temperature rise. The fault in the cooling period was applied at the period midpoint. In healthy conditions, the FBG-AF is seen to report a thermal profile closely similar to those read by other sensors. From the outset of fault however, the FBG-AF readings show an extreme temperature rise in both the heating and cooling period fault instances. This originates from additional, fault-induced, rise in thermal loss in the slot and follows the principles discussed in Section IV, but now in dynamic conditions: Upon removal of fault, this additional

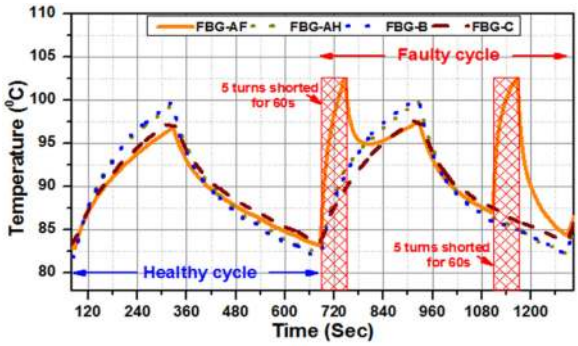

Fig. 12. Thermal measurements in dynamic conditions, five turns shorted fault.

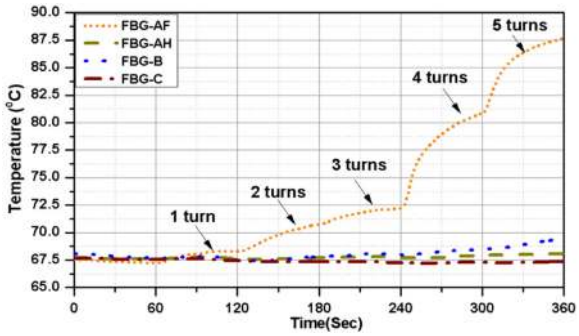

Fig. 13. Measured temperature profile under fault propagation.

thermal loss is removed and the measured temperature is seen to gradually return to its healthy cycle form after a cool down period. Monitoring the discussed fault-induced thermal rise can enable unambiguous fault diagnosis.

Thermal signature based fault detection is more straightforward in the cooling period, as all sensors report a temperature decrease while the sensor in the faulty slot reports a temperature rise. In the heating transient, the *in situ* sensor shows high sensitivity in recognition of fault-induced thermal stress. The experimental data demonstrate the capability of incipient ITSCF thermal fault signature recognition by the proposed *in situ* thermal monitoring scheme in transient conditions.

C. Fault Severity Trending

The breakdown of the winding is the final stage of ITSCFs, and is typically reached after a series of stages of fault propagation [6]. Effectively monitoring the fault propagation stages to extract knowledge of machine operational status is an underlying requirement for useful diagnostic systems. It has been shown in the previous sections that different ITSCF severities generate different levels of thermal stress and hence, different levels of fault thermal signature, which can be used as an indicator of the fault propagation stage.

In this section, experimental work was performed in order to investigate the capability of the *in situ* FBG sensor to recognize the ITSCF propagation stages. A test was performed to emulate an ITSCF propagation scenario comprising five distinct stages, starting with a single turn fault and increasing to five shorted turns fault in steps of one turn fault. Each fault stage was maintained for a period of 60 s in the test before introducing the following fault stage. The test commences after the thermal equilibrium of the winding was reached in no-load conditions. Fig. 13 shows the measured temperature profiles obtained by the four FBGs for the applied fault scenario. The measurements demonstrate that the proposed *in situ* thermal monitoring system is able to provide clear recognition of fault status and its propagation signature: At each fault stage, the FBG-AF reports a different, distinct temperature level. The faulty coil side hot spot temperature increases with fault propagation from ≈67.5 °C at healthy conditions to reach ≈88 °C at 5 turns fault stage. Another attractive advantage of the proposed diagnostic technique is that it does not require complex real-time algorithms for interpretation of fault signature, such as needed with electromagnetic signal signature analysis techniques [3].

V. Conclusion

This paper reported a new technique for ITSCF on-line diagnosis in random wound machines based on fully EMI immune FBG sensor *in situ* monitoring of winding internal thermal excitation. The proposed scheme was implemented and its performance was validated on an inverter-driven induction motor. The study focuses on the detection of the early stages of ITSCF, where other techniques largely present limited success.

The reported findings demonstrated that the presented scheme could provide reliable diagnosis of ITSCF including, detection of ITSCF at earliest stages (i.e., single turn), fault severity diagnosis, and a straightforward identification of fault location. The winding *in situ* thermal sensing network required to underpin this diagnostics can readily be achieved utilizing FBG multiplexing features in a single fiber array sensor. The results and analysis in this paper enable full understanding of the FBG monitoring principles required for practical establishment of such a scheme.

The proposed *in situ* FBG thermal sensing for ITSCF detection provides advantages over existing diagnostic techniques in steady state and in particular in transient conditions, as no complex real-time processing is required for fault signature diagnostic interpretation. The manifestation of the observed fault-induced thermal phenomena is generally expected to be dependent on machine design class.

References

[1] S. Grubic, J. M. Aller, B. Lu, and T. G. Habetler, "A survey on testing and monitoring methods for stator insulation systems of low-voltage induction machines focusing on turn insulation problems," *IEEE Trans. Ind. Electron.*, vol. 55, no. 12, pp. 4127–4136, Dec. 2008.

[2] G. N. Surya, Z. J. Khan, M. S. Ballal, and H. M. Suryawanshi, "A simplified frequency-domain detection of stator turn fault in squirrel-cage induction motors using an observer coil technique," *IEEE Trans. Ind. Electron.*, vol. 64, no. 2, pp. 1495–1506, Feb. 2017.

[3] A. Gandhi, T. Corrigan, and L. Parsa, "Recent advances in modeling and online detection of stator interturn faults in electrical motors," *IEEE Trans. Ind. Electron.*, vol. 58, no. 5, pp. 1564–1575, May 2011.

[4] F. Çira, M. Arkan, B. Gümüş, and T. Goktas, "Analysis of stator interturn short-circuit fault signatures for inverter-fed permanent magnet synchronous motors," in *Proc. 42nd Annu. Conf. IEEE Ind. Electron. Soc.*, Florence, Italy, 2016, pp. 1453–1457.

[5] D. G. Dorrell and K. Makhoba, "Detection of inter-turn stator faults in induction motors using short term averaging of forwards and backwards rotating stator current phasors for fast prognostics," *IEEE Trans. Magn.*, vol. 53, no. 11, Nov. 2017, Art. no. 1700107.
[6] J.-K. Park and J. Hur, "Detection of inter-turn and dynamic eccentricity faults using stator current frequency pattern in IPM-type BLDC motors," *IEEE Trans. Ind. Electron.*, vol. 63, no. 3, pp. 1771–1780, Mar. 2016.
[7] V. Nguyen, J. Seshadrinath, D. Wang, S. Nadarajan, and V. Vaiyapuri, "Model-based diagnosis and RUL estimation of induction machines under inter-turn fault," *IEEE Trans. Ind. Appl.*, vol. 53, no. 3, pp. 2690–2701, May/Jun. 2017.
[8] C. Gerada *et al.*, "The results do mesh," *IEEE Ind. Appl. Mag.*, vol. 13, no. 2, pp. 62–72, Mar./Apr. 2007.
[9] G. M. Joksimovic and J. Penman, "The detection of inter-turn short circuits in the stator windings of operating motors," *IEEE Trans. Ind. Electron.*, vol. 47, no. 5, pp. 1078–1084, Oct. 2000.
[10] M. Riera-Guasp, J. A. Antonino-Daviu, and G.-A. Capolino, "Advances in electrical machine, power electronic, and drive condition monitoring and fault detection: state of the art," *IEEE Trans. Ind. Electron.*, vol. 62, no. 3, pp. 1746–1759, Mar. 2015.
[11] G. Singh, T. C. A. Kumar, and V. N. A. Naikan, "Induction motor inter turn fault detection using infrared thermographic analysis," *Infrared Phys. Technol.*, vol. 77, pp. 277–282, 2016.
[12] A. Glowacz and Z. Glowacz. "Diagnosis of the three-phase induction motor using thermal imaging," *Infrared Phys. Technol.*, vol. 81, pp. 7–16, 2017.
[13] A. G. Garcia-Ramirez *et al.*, "Fault detection in induction motors and the impact on the kinematic chain through thermographic analysis," *Electric Pow. Syst. Res.*, vol. 114, pp. 1–9, 2014.
[14] R. M. Tallam, T. G. Habetler, and R. G. Harley, "Experimental testing of a neural-network-based turn-fault detection scheme for induction machines under accelerated insulation failure conditions," in *Proc. 4th IEEE Int. Symp. Diagnostics Electr. Machines, Power Electron. Drives*, 2003, pp. 58–62.
[15] M. G. Melero *et al.*, "Study of an induction motor working under stator winding inter-turn short circuit condition," in *Proc. 4th IEEE Int. Symp. Diagnostics Electric Mach., Power Electron. Drives,* 2003, pp. 52–57.
[16] W. T. Thomson, "On-line MCSA to diagnose shorted turns in low voltage stator windings of 3-phase induction motors prior to failure," in *Proc. IEEE Int. Electr. Machines Drives Conf.*, Cambridge, MA, USA, 2001, pp. 891–898.
[17] F. Marignetti et al., "Fiber Bragg grating sensor for electric field measurement in the end windings of high-voltage electric machines," *IEEE Trans. Ind. Electron.*, vol. 63 no. 5, pp. 2796–2802, May 2016.
[18] J. M. Corres, J. Bravo, F. J. Arregui, and I. R. Matias, "Unbalance and harmonics detection in induction motors using an optical fiber sensor," *IEEE Sensors J.*, vol. 6, no. 3, pp. 605–612, Jun. 2006
[19] M. Fabian, M. Ams, C. Gerada, T. Sun, and K. T. V Grattan, "Vibration measurement of electrical machines using integrated fibre Bragg gratings." in *Proc. Int. Conf. Opt. Fibre Sensors*, 2015, pp. 1–4.
[20] R. C. Leite *et al.*, "Analysis of thermo-mechanical stress in fiber Bragg grating used for generator rotor temperature monitoring," *J. Microw. Optoelectron. Electromagn. Appl.*, vol. 16, no. 3, pp. 445–459, 2017.
[21] K. D. M. Sousa, A. A. Hafner, and J. C. C. da Silva, "Determination of temperature dynamics and mechanical and stator losses relationships in a three-phase induction motor using fiber Bragg grating sensors," *IEEE Sens. J.*, vol. 12, no. 10, pp. 3054–3061, Oct. 2012.
[22] A. Mohammad and S. Djurović, "A study of distributed embedded thermal monitoring in electric coils based on FBG sensor multiplexing," *Microprocessors Microsystems*, vol. 62, pp. 102–109, 2018.
[23] A. Mohammed and S. Djurović, "Stator winding internal thermal stress monitoring and analysis using in-situ FBG sensing technology," *IEEE Trans. Energy Convers.*, vol. 33, no. 3, pp. 1508–1518, Sep. 2018.
[24] A. Mohammed and S. Djurović, "FBG thermal sensing features for hot spot monitoring in random wound electric machine coils," *IEEE Sensors J.*, vol. 17, no. 10, pp. 3058–3067, May 2017.
[25] Smartfibres.com., *Smart Fibres | Pioneering Opt. Fibre Sens.*. (2017). [Online]. Available: http://www.smartfibres.com
[26] Z. Gao *et al.*, "Active monitoring and vibration control of smart structure aircraft based on FBG sensors and PZT actuators," *Aerosp. Sci. Technol.*, vol. 63, pp. 101–109, 2017.
[27] W. Ecke and K. Schröder, "Fiber Bragg grating sensor system for operational load monitoring of wind turbine blades," *Proc. SPIE*, vol. 6933, 2008, Art. no. 69330I.
[28] P. J. Tavner, "Review of condition monitoring of rotating electrical machines," *IET Electric Power Appl.*, vol. 2, no. 4, pp. 215–247, 2008.
[29] *Rotating Electrical Machines—Part 1: Rating And Performance*, IEC 60034-1:2010.
[30] K. Tshiloz, A. C. Smith, A. Mohammed, S. Djurović, and T. Feehally, "Real-time insulation lifetime monitoring for motor windings," in *Proc. 22nd Int. Conf. Elect. Mach.,* Lausanne, Switzerland, 2016, pp. 2335–2340.
[31] F. J. T. E. Ferreira, B. Leprettre, and A. T. de Almeida, "Comparison of protection requirements in IE2-, IE3-, and IE4-class motors," *IEEE Trans. Ind. Appl.*, vol. 52, no. 4, pp. 3603–3610, Jul./Aug. 2016.

Anees Mohammed (S'15) received the M.Sc. degree in electrical power engineering from the University of Newcastle, U.K., in 2010. He is currently working toward the Ph.D. degree in electrical and electronic engineering at the University of Manchester, Manchester, U.K.

He has spent four years working as an Assistant Lecturer with Benghazi University, Benghazi, Libya. His research interests include electric machines, drives, and condition monitoring.

Juan I. Melecio received the B.S. degree in mechatronics engineering and the M.Sc. degree in energy engineering from Tecnológico de Monterrey, Monterrey, Mexico, in 2008 and 2010, respectively. He is currently working toward the Ph.D. degree in electrical and electronic engineering at the University of Manchester, Manchester, U.K.

He has spent five years working with Schneider Electric in Monterrey, Mexico, and Cedar Rapids, IA, USA. His research interests include finite-element analysis, electrical machines, drives, and condition monitoring.

Siniša Djurović (M'09) received the Dipl.Ing. degree in electrical engineering from the University of Montenegro, Podgorica, Montenegro, in 2002, and the Ph.D. degree in electrical machine modelling and fault analysis from the University of Manchester, Manchester, U.K., in 2007.

He is currently a Senior Lecturer with the Power Conversion Group at Manchester, U.K. His research interests include the area of operation, design, monitoring, and diagnostics of electric machines and drives.